

## An Algorithm for Real-Time Optimal Photocurrent Estimation including Transient Detection for Resource-Constrained Imaging Applications

Michael Zemcov<sup>1,2,†</sup>, Brendan Crill<sup>2</sup>, Matthew Ryan<sup>2</sup>, Zak Staniszewski<sup>2</sup>

<sup>1</sup>Center for Detectors, School of Physics and Astronomy, Rochester Institute of Technology, Rochester, NY 14623, USA,  
zemcov@afd.rit.edu

<sup>2</sup>Jet Propulsion Laboratory, Pasadena, CA 91109, USA

Received 2016 April 5; Revised 2016 May 6; Accepted 2016 May 18

Mega-pixel charge-integrating detectors are common in near-IR imaging applications. Optimal signal-to-noise ratio estimates of the photocurrents, which are particularly important in the low-signal regime, are produced by fitting linear models to sequential reads of the charge on the detector. Algorithms that solve this problem have a long history, but can be computationally intensive. Furthermore, the cosmic ray background is appreciable for these detectors in Earth orbit, particularly above the Earth's magnetic poles and the South Atlantic Anomaly, and on-board reduction routines must be capable of flagging affected pixels. In this paper we present an algorithm that generates optimal photocurrent estimates and flags random transient charge generation from cosmic rays, and is specifically designed to fit on a computationally restricted platform. We take as a case study the Spectro-Photometer for the History of the Universe, Epoch of Reionization, and Ices Explorer (SPHEREx), a NASA Small Explorer astrophysics experiment concept, and show that the algorithm can easily fit in the resource-constrained environment of such a restricted platform. Detailed simulations of the input astrophysical signals and detector array performance are used to characterize the fitting routines in the presence of complex noise properties and charge transients. We use both Hubble Space Telescope Wide Field Camera-3 and Wide-field Infrared Survey Explorer to develop an empirical understanding of the susceptibility of near-IR detectors in low earth orbit and build a model for realistic cosmic ray energy spectra and rates. We show that our algorithm generates an unbiased estimate of the true photocurrent that is identical to that from a standard line fitting package, and characterize the rate, energy, and timing of both detected and undetected transient events. This algorithm has significant potential for imaging with charge-integrating detectors in astrophysics, earth science, and remote sensing applications.

*Keywords:* methods: data analysis, space vehicles: instruments, techniques: image processing

### 1. Introduction

Modern infrared detectors have multi-mega pixel formats (Beletic *et al.*, 2008), so can produce large data volumes in short times (*e.g.* Smith & Hale 2012). This is problematic in space applications, where data telemetry is expensive. This problem is typically solved by using some form of Correlated Double Sampling (CDS; Fowler & Gatley 1990, *e.g.* Robberto 2007), which permits the information from multiple reads of a detector during a single integration to be summarized by a single total pixel number  $N_{\text{pix}}$ -sized frame. In contrast, “Sample Up the Ramp” (SUR) methods offer larger signal-to-noise ratios in a given integration time (Garnett & Forrest, 1993), as well as the ability to identify and reject cosmic ray and other transient events, at the cost of significantly increased data volumes (Rauscher *et al.*, 2007). In order to implement SUR algorithms in telemetry-constrained applications, some amount of data processing and reduction must be performed on-board.

As a specific application, we have studied these algorithms for use in the Spectro-Photometer for the History of the Universe, Epoch of Reionization, and Ices Explorer (SPHEREx<sup>1</sup>; Doré *et al.* 2014). SPHEREx

---

<sup>†</sup>Corresponding author.

<sup>1</sup><http://spherex.caltech.edu>

is a proposed Small Explorer mission designed to generate  $\lambda/\Delta\lambda = 41.5$  spectra for  $0.75 < \lambda < 4.1\mu\text{m}$  and  $R = 150$  spectra for  $4.1 < \lambda < 4.8\mu\text{m}$  for every 6.2 arcsecond pixel over the entire sky. It will utilize four H2RG detectors read out using SIDECAR ASICs (Loose *et al.*, 2006) in 32-channel mode driven at a  $\sim 1.5\text{s}$  sample rate. To cover the entire spectral band, we will use two  $2.5\mu\text{m}$  and two  $5\mu\text{m}$  optimized detectors operating at  $\gtrsim 50\text{K}$ . Similar systems are planned to be deployed on upcoming large missions like the James Webb Space Telescope (JWST; Rauscher *et al.* 2007) and Euclid (Crouzet *et al.*, 2012), allowing us to leverage existing characterization studies to predict the performance of SPHEREx. Because of the narrow spectral window passed to the detectors, we expect median photocurrents  $\lesssim 1\text{e}^- \text{s}^{-1}$  per pixel. As a result, it is crucial to optimize the signal-to-noise ratio per integration, leading the SPHEREx team to baseline the SUR algorithm, which has the added benefit of providing robustness against detector transients.

The streamlined and efficient nature of Small Explorer<sup>2</sup> class missions necessitates the use of high-heritage, resource-constrained processing platforms, restricting the possible scope of on-board data processing algorithms. For similar reasons, the data telemetry bandwidth is constrained, which places a premium on data reduction compression. These competing requirements impose a significant challenge: we need to maximally reduce the transmitted data volume, while allocating the reduction processing minimal resources. This paper presents our solution to this problem, which takes the form of a set of resource-constrained algorithms that: (i) return the optimal SUR photocurrent estimate; (ii) allow real-time transient flagging; and (iii) minimize the required long term data storage and telemetry bandwidth. The paper is organized as follows: in Sec. 2 we summarize the expected characteristics of the SPHEREx data as they relate to the on-board processing. We present the data reduction algorithms in Sec. 3, and then show a variety of characterization and validation tests in Sec. 4. In Sec. 5, we present details of the hardware implementation of the SPHEREx flight system, and show that the algorithms fit within the available resource envelope. Finally, we discuss broader implications of this work in Sec. 6.

## 2. Data Description

The SPHEREx H2RG detector arrays are *charge-integrating*, which is to say, incident photons generate a current in the detector material that is proportional to the photon flux. However, it is the charge on the detector pixels that is amplified and digitized by the readout system. The photon signal is therefore proportional to the derivative of the measured charge on the detector over time, which leads to the SUR estimate for the signal intensity. The current at the detector  $i_{\text{phot}}$  can be related to the intensity of the astrophysical signal  $\lambda I_{\lambda}$  via:

$$i_{\text{phot}} \simeq \lambda I_{\lambda} \left( \frac{\eta A \Omega \Delta \lambda}{h \nu \lambda} \right), \quad (1)$$

where  $A\Omega$  is the pixel throughput,  $\eta$  is the total efficiency, and  $\Delta\lambda$  is the integral bandwidth (*e.g.* Bock *et al.* 2013). As a result, SPHEREx operates in a point-and-stare observational mode. The dominant astrophysical signal in an average array pixel is due to Zodiacal Light (ZL) which has a known brightness versus wavelength (Kelsall *et al.*, 1998), allowing us to tailor our integration lengths to be photon-noise limited. In this study, we baseline the all-sky survey integration time  $T_{\text{int}}$  per field to be  $\sim 107\text{s}$  per pointing so that the photocurrent noise is always dominated by shot noise from photons. Given this  $T_{\text{int}}$ , the spectral resolution of the instrument, and the orbit, it is possible to calculate an observation sequence that will tile the entire sky in six months (Spangelo *et al.*, 2015).

A given observation consists of a slew to the target field, an array charge reset, integration on the target for  $T_{\text{int}}$ , followed by an array reset and then a slew to the next target. During the integration, charge values are sequentially read from the array with a  $\Delta t = 1.5\text{s}$  pixel visit cadence and accumulated into various sums (see Sec. 3). At the end of the integration, the algorithm solves for the photocurrent, compresses the output, and stores it to disk. An schematic time series is shown in Fig. 1, highlighting the sequence.

---

<sup>2</sup><http://explorers.gsfc.nasa.gov/smex.html>

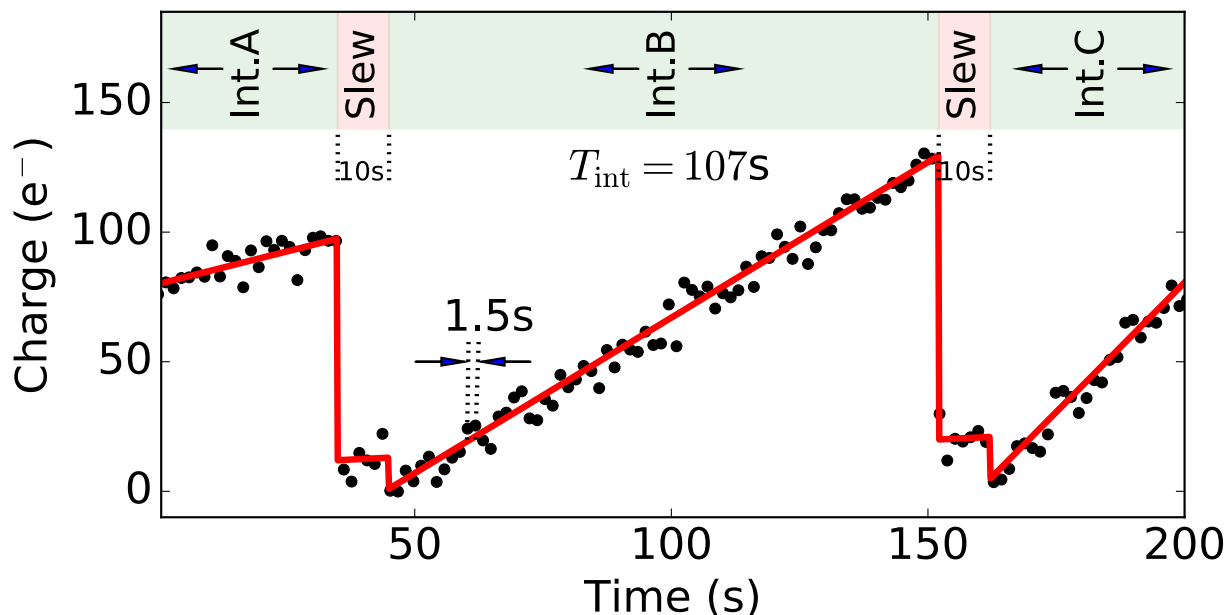


Fig. 1. Schematic view of a typical SPHEREx observing sequence. The plot shows the end of an observation (‘Int. A’), a slew to a new target, a full 107s integration (‘Int. B’), a slew to a third target, and the beginning of a third integration (‘Int. C’). Data samples are indicated with a 1.5s sample rate (black points), and the input photocurrent in each section is also shown (red line). The steps at the beginning and end of each integration are due to detector resets.

H2RG detectors exhibit a rich phenomenology of noise that has already been well studied. Rauscher (2015) has built code for a noise model which captures much of the salient phenomenology (see Sec. 4.1 for details). In this work, we assume the SPHEREx arrays have the parameters shown in Table 1. Missing from this model and required to complete our tests is a model for cosmic ray events, which can have a large effect above the shielding of the earth’s atmosphere.

Table 1. Assumed H2RG array parameters.

| Parameter                               | Value                        |
|---|------------------------------|
| Array type                              | Teledyne H2RG                |
| Array format                            | 2048 × 2048 pixels           |
| Output mode                             | 32 channel                   |
| Frame read rate                         | 1.5 s                        |
| Dark current $i_d$                      | 5 $me^- s^{-1}/\text{pixel}$ |
| Read noise                              | 5.2 $e^-$                    |
| DC pedestal drift rms                   | 4 $e^-$                      |
| Correlated pink noise rms               | 3 $e^-$                      |
| Uncorrelated pink noise rms             | 1 $e^-$                      |
| Correlated alternating column noise rms | 0.5 $e^-$                    |
| Equivalent CDS rms                      | 10.5 $e^-$                   |

### 2.1. Cosmic Ray Rate and Spectrum

There is little data available on the *in situ* cosmic ray susceptibility of modern, large-format HgCdTe arrays deployed in space. No instrument currently in flight uses H2RG-class detectors; however, both the Hubble Space Telescope (HST) Wide-Field Camera-3 (WFC-3; Dressel 2016) and the Wide-field Infrared Survey Explorer (WISE; Wright *et al.* 2010) instruments use H1RG detectors, which are essentially a single quadrant of an H2RG detector. In addition, the mean altitudes of both HST (560 km) and WISE (525 km)

Table 2. Data sets used in the WFC-3 cosmic ray study.

| Field Type | Acquisition Dates | Number of files | Reads per file | Integration time per read ( $dt$ ) | Total exposure time |
|------------|-------------------|-----------------|----------------|------------------------------------|---------------------|
| Regular    | 2009 - 2016       | 140             | 14             | 200 s                              | 2800 s              |
| SAA        | Jun. -Jul. 2009   | 84              | 3              | 50 s                               | 150 s*              |

\* The integration time in the SAA region is necessarily shorter as HST passes through the region on a similar time scale.

are similar but slightly lower than that predicted for SPHEREx (600 km), putting them in comparable regions of the earth’s radiation belts. Finally, both the WFC-3 and SPHEREx detectors are substrate-removed, ensuring the cosmic ray cross-sections are similar.

Of course, there are complications to this comparison, not least of which is the difference in cosmic ray shielding between WFC-3, WISE, and SPHEREx. However, without a detailed physical model of the instruments that models the material properties, geometries, *etc.*, it is not possible to account for these differences. For the purpose of this study, we choose to neglect these differences. As shown below, the cosmic ray rates are low enough that even an order of magnitude error from this assumption would typically have a negligible effect on the SPHEREx survey.

To complete this study, we have used a set of dark data both in “regular” regions of the earth’s magnetic field, and while in the South Atlantic Anomaly (SAA), a region in the magnetosphere where cosmic ray event rates are known to be dramatically higher. The data sets are summarized in Table 2. For this study, we use offset-subtracted array reads separated by a given time per read, calibrated to  $e^- s^{-1}$  using known gain factors.

The data analysis proceeds assuming a simple model for cosmic ray events. Pixels (which in this case have no external illumination) have a small linear ramp with time corresponding to the dark current, which is  $\sim me^- s^{-1}$  for this detector. The read noise is much larger than this, on the order of electrons, so a typical pixel’s time stream is effectively just noise with approximately no gradient. This means the array currents should be well modeled by a histogram with mean very close to zero, and shape symmetric about that mean<sup>3</sup>. To isolate the photocurrent, we subtract the first frame read from the last, which removes instrumental offsets. The result, when corrected for the integration time, is the charge accumulated on a detector over the exposure time. The effect of cosmic rays is to skew the positive-going side of a histogram of the array pixel values to larger values.

Pathological pixels are problematic for this analysis as they can deviate strongly from the behavior of a normal pixel, and could look like either (a) strongly negative-going events, which would skew our estimate of the non-white component of the noise, or (b) strongly positive-going events, appear to be cosmic rays. In fact, the number of pathological pixels could be much larger than the typical number of cosmic ray events, so these must be eliminated. To develop a bad pixel mask, we perform an analysis where we compute differences between randomly selected exposure pairs. Bad pixels are those defined as *always* displaying a pathology, so should be the same between exposures separated by a random amount of time. We perform this procedure with a selection of 10 random pairings without replacement, and require that bad pixel candidates are flagged in a minimum of two different data set pairs to be flagged as bad in the final mask. From this selection, we form a pixel mask that should have identified most of the pathological pixels in the detector. In all, 1.7% of pixels are flagged and ignored in the following analysis.

Having flagged bad pixels, we can compute histograms of the remaining pixels to find cosmic ray hits, shown in Fig. 2, including models for the Gaussian and power law-like noise terms. As the detector noise should be symmetric about the mean, the power law derived from the negative-going data should also match the positive-going side. In both the non-SAA and SAA cases, an excess of positive-going events is evident at  $q \gtrsim 100 e^-$ , which we associate with cosmic ray events.

To isolate these cosmic ray events, we subtract the noise model curve from the histogram. In Fig. 3 we show the resulting energy spectrum for cosmic rays as measured in the two data sets. The regular region data are remarkably consistent, and follow a smooth power law model. The SAA region data are less

<sup>3</sup>Note it is not necessary to assume that the noise properties are particularly well-behaved: we only require noise pathologies occur in both the positive-charge and negative-charge directions equally.

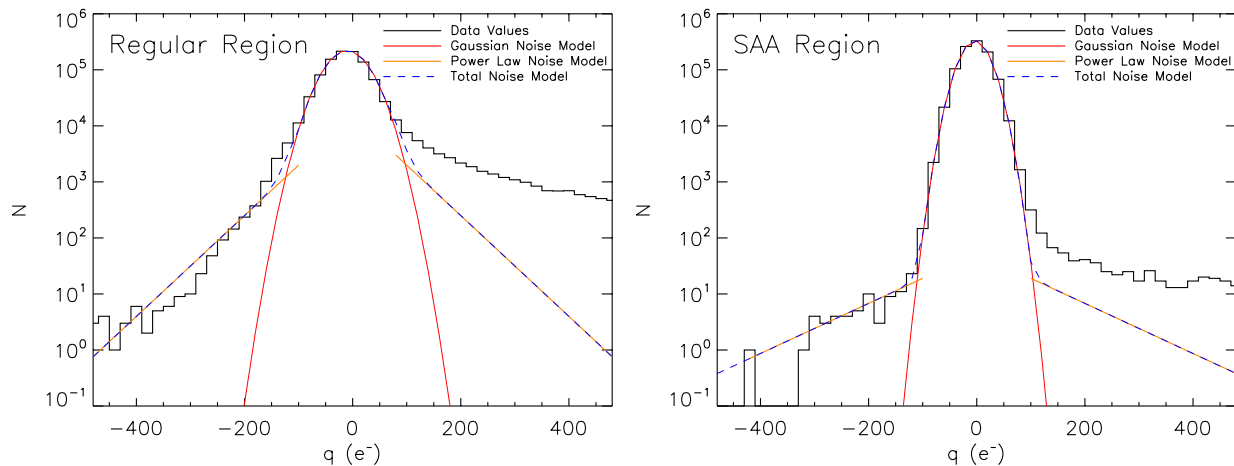


Fig. 2. Histograms of the pixel values for two files typical of the SAA and regular regions. The two data sets have been scaled to the common SAA integration time of 150 s. This has the effect of causing the white-noise component width to be the same between the two sets, but increases the relative contribution of rare events in the non-SAA data. Also shown are a Gaussian model for the quasi-white noise contribution (solid red line) with an rms noise of  $\sim 24 e^-$  (corresponding to  $\sim 150 me^-/s$ ). To account for the non-Gaussian population of pixels creating the negative-going wing, we fit a power law model (yellow line), and also show the sum of the noise components (blue line). Assuming that the non-Gaussian noise component is equal in both the negative- and positive-going directions, the excess of the histogram on the positive-going side over the power law term is due to cosmic ray events.

consistent, but the lowest-event rate sets are very similar to the regular region data. There are, however, large outlier events that are not rare. It is not possible from these data alone to determine how these outlier data sets correlated with external factors such as path through the SAA or solar activity, though it is probably a reasonable assumption that such correlation is present. From these data, we determine an event rate that is  $1.3 \times 10^{-4}$  events  $s^{-1}$  pixel $^{-1}$ , consistent with previous analyses of similar data (Barker *et al.*, 2010).

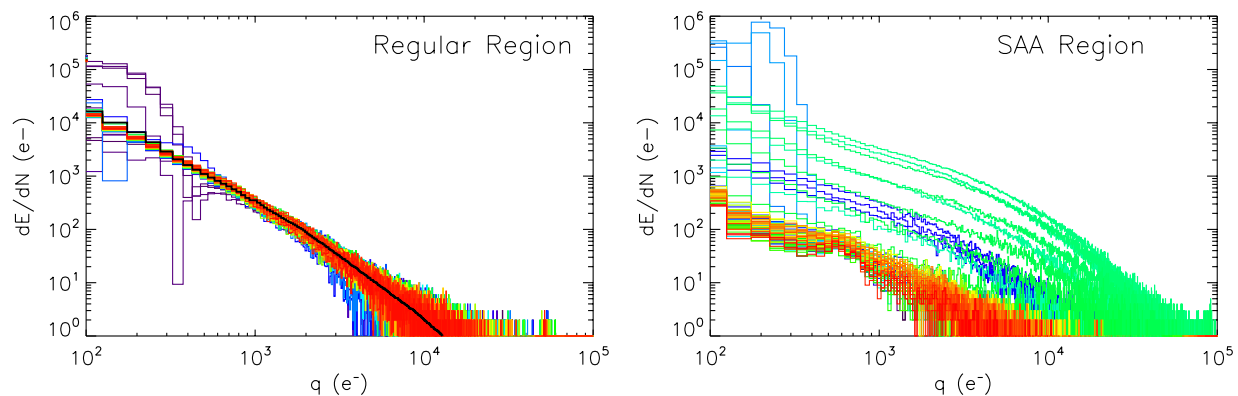


Fig. 3. Cosmic ray energy spectra for both regular and (left panel) and SAA regions (right panel). Colors correspond to data set number, given in Table 2.

Though the WFC-3 detector is a good analog to those of SPHEREx, HST does not follow a polar orbit, and as a result does not pass through the earth's magnetic poles. These may trap cosmic rays similarly to the SAA region, and potentially could have an even larger event rate or more energetic spectrum. To place limits on this, we use cosmic ray hit data from WISE, which follows a very similar earth-terminator orbit to SPHEREx. These data give cosmic ray event rates over the full sky at a 535 km altitude near

beginning of the WISE mission. The WISE event rates are qualitatively consistent with those of WFC-3 in the SAA. Scaling to the SPHEREx integration time, we would expect  $\sim 1\%$  percent of pixels to suffer from detectable events when within 30 degrees of latitude of each pole, corresponding to  $1/6^{\text{th}}$  of an orbit, is a modest increase in the total number of events over the baseline expectation.

### 3. Data Processing Algorithm

The algorithm described here is developed from the “normal equation” formalism<sup>4</sup> (see *e.g.* Press *et al.* 1992 chapter 15 for a review), and shares common heritage with algorithms developed to address similar requirements in previous NASA flight projects (Fixsen *et al.* 2000, Offenberg *et al.* 2005). Because of the limited resources available to SPHEREx, we have developed this algorithm to optimize against the following metrics:

- (1) *Return the optimal<sup>5</sup> best-fitting photocurrent, while*
- (2) *robustly detecting cosmic rays and other transients, and simultaneously*
- (3) *minimizing RAM requirements, and*
- (4) *minimizing the number of computations.*

We place no emphasis on returning accurate error estimates for the fits, or for retrieving the full-integration slope in cosmic ray-affected pixels using a constrained fit model<sup>6</sup>.

#### 3.1. Processing Architecture

The overall architecture of the on-board processing pipeline for SPHEREx is summarized in Fig. 4. At each time sample for each pixel, the data is loaded into the on-board RAM. Next, the algorithm checks for transient events and detector saturation using the algorithms detailed in the next section. Finally, various quantities are computed and updated before the next sample arrives. Following the accumulation of a full integration, the SUR estimate is computed using the summed information and pre-computed look-up values. For SPHEREx, we are concerned about the performance of the on-board processing algorithms over the lifetime of the mission, so also append the full time series for an  $8 \times 32$  sub-image in each of the 4 H2RG detector arrays. This sub-array information can be analyzed in detail during later analysis and the results compared against the in-flight processing results to monitor the algorithm performance. This is also useful for determining the cosmic ray hit rate and energy spectrum in the as-built instrument, as well as checking the pixel performance stability over the lifetime of the mission. Finally, the data set comprising the SUR image, flags, and diagnostic data are compressed and moved to storage for later telemetry to the ground station.

#### 3.2. SUR Photocurrent Estimates

In the most general form, a linear relationship between the photocurrent  $\partial q/\partial t$  and reads of the charge on the detector  $q$  can be written as:

$$q_i = A_{ij} \cdot m_j + n_i \quad (2)$$

where  $i$  corresponds to sample number,  $j$  to pixel number,  $m_0 = f \propto \partial q/\partial t$  is the incident flux in suitable units,  $m_1 = q_0$  the initial charge on the detector,  $A_{ij}$  the  $i \times 2$  design matrix<sup>7</sup> encoding the linear transform, and  $n_i$  is a random number drawn from a suitable probability density function (PDF) to match the statistics

<sup>4</sup>So named because the equations specify that the residual must be normal to every vector in the span of  $A$ .

<sup>5</sup>Here we use “optimal” in the sense of maximum signal-to-noise ratio in a given integration time, rather than providing an optimal estimate of the *error* in the fit parameters.

<sup>6</sup>This is in contrast to *e.g.* Offenberg *et al.* (2005) where the on-board processing algorithm is designed with these considerations in mind.

<sup>7</sup>In statistics, a “design matrix” is a matrix of explanatory variables of a set of objects. In this particular instance, each row represents an individual time sample, with the successive columns corresponding to pixel samples at that time.

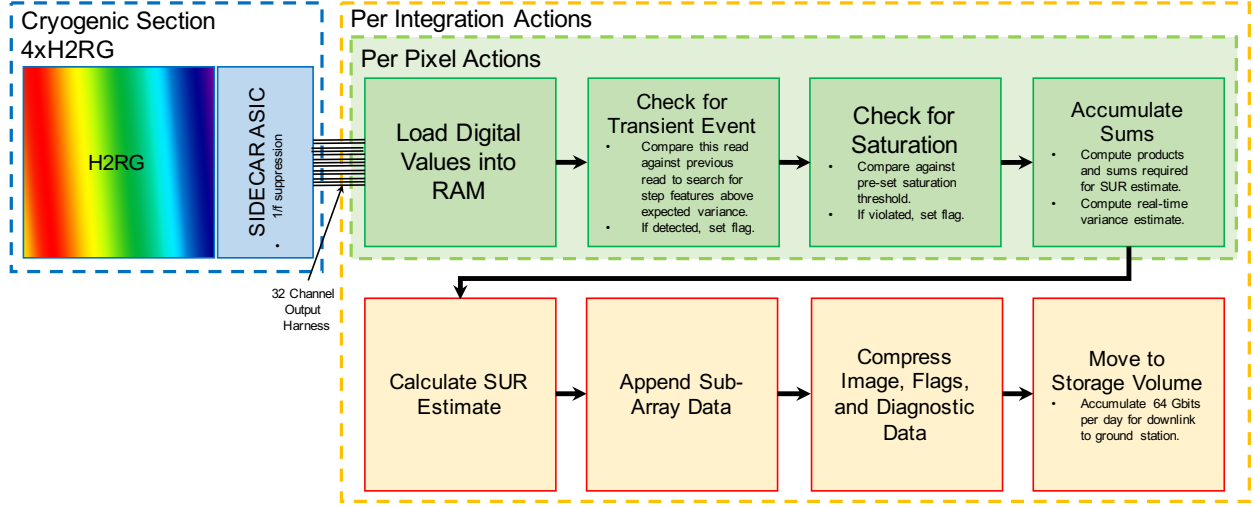


Fig. 4. On-board data processing flow for SPHEREx. For each detector, data is sampled from the H2RG using 32 output channels and loaded into RAM on the processing board. At each time step, we check and flag for time stream transient events and pixel reciprocity failure before accumulating various quantities (see Sec. 3.2). At the end of each integration, these quantities are then used to build optimal estimates for the photocurrent in each detector. A  $8 \times 32$  pixel sub-array sampled at full time resolution is appended to the image and flag data, which are then compressed. These are then shifted to a storage volume for later transmission to the ground station.

of the physical process at hand (here the sum of photon noise and read noise, which can potentially be arbitrarily complex functions of  $f$  and  $q$ ). In a fitting problem, we want to solve for the value of  $m$ , which is given by:

$$m = (A^T N^{-1} A)^{-1} A^T N^{-1} q, \quad (3)$$

where  $A$  is the design matrix,  $^T$  is the transpose operation, and  $N$  is the noise covariance matrix computed from  $n$ .

To simplify the most general solution, we can take advantage of the fact that SPHEREx will stare at an observation field with a fixed sampling cadence and pre-determined  $T_{\text{int}}$ . Because most pixels will have photocurrents  $\sim 1 e^- s^{-1}$ , the noise term will be close to constant in a given integration (see Sec. 4.2.1). This allows us to set  $\sigma_i^2 = \sigma_j^2$  so the matrix is diagonal. This means that the  $N$  terms appear as factors of  $\sigma^{-2}$  in the  $(A^T N^{-1} A)^{-1}$  and factors of  $\sigma^2$  in the  $A^T N^{-1}$  term, and cancel. Thus  $N$  drops from the problem.

The fixed sampling cadence imposes a well-defined, regular structure on the design matrix, while the pre-defined integration time means the design matrix's ultimate size is known. The structure of the design matrix is:

$$A = \begin{bmatrix} 0 & 1 \\ 1 & 1 \\ 2 & 1 \\ \vdots & \vdots \\ n-1 & 1 \end{bmatrix} = [i, 1] \quad (4)$$

where  $n$  is the number of points in the integration. As a result, the term  $(A^T A)$  is simply a  $(2 \times 2)$  matrix composed as:

$$(A^T A) = \begin{bmatrix} \sum_0^{n-1} A_{0i}^2 & \sum_0^{n-1} A_{0i} \\ \sum_0^{n-1} A_{0i} & \sum_0^{n-1} 1 \end{bmatrix} \quad (5)$$

To solve Equation 3, we need to compute  $(A^T A)^{-1}$  from this. Each computation of this matrix requires a product and four sums per sample, as well as a inversion once the full matrix accumulated. However, we

can take advantage of our prior knowledge of the problem to pre-compute the solution at a given  $T_{\text{int}}$  and store it in RAM. For every possible integration time up to 300s, we would only require 25.6 kbits to store every possible matrix inverse as a lookup, which is negligible compared to other RAM requirements.

For the  $A^T q$  term, we note again the structure of  $A$ , which causes this term to simplify to:

$$(A^T q) = [\sum_0^{n-1} A_{0i} q_i \sum_0^{n-1} q_i] \quad (6)$$

Of course, since  $A_{0i} = i$  this simplifies further to:

$$(A^T q) = [\sum_0^{n-1} i q_i \sum_0^{n-1} q_i] \quad (7)$$

To compute  $(A^T q)$  in Equation 3, we simply need to compute two terms: the sum of the product of the frame number and the data point at that frame, and the sum of the data points. At the end of the integration, we can multiply these by the pre-computed  $(A^T A)^{-1}$  lookup to solve for  $m$ .

The resource requirements for this formalism are thus:

- (1) The frame number  $i$ . This can be shared by all fits as a global 8-bit integer.
- (2) A cumulative sum of the product of  $i$  and  $q_i$  for each pixel, with size  $4 \times 2048 \times 2048 \times 32$  bits.
- (3) A cumulative sum of  $q_i$  for each pixel, with size  $4 \times 2048 \times 2048 \times 32$  bits.

At the end of the integration, we multiply these cumulants by the pre-computed inverse design matrix to compute  $\partial q/\partial t$  per pixel, requiring  $2 \times 4 \times 2048 \times 2048$  multiplies and  $4 \times 2048 \times 2048$  adds and resulting in a matrix with size  $4 \times 2048 \times 2048 \times 32$  bits.

### 3.3. Transient Detection

Though cosmic rays, electronics glitches, *etc.* arise from different physical processes, they all lead to step discontinuities in the detector time streams. These can be detected *a posteriori* by determining goodness-of-fit statistics, but the computational and memory burdens of such computations are large. Here we implement a “transient detector” algorithm that searches for step discontinuities in real time and flags data points which exceed some threshold from the expected linear trend for the detector. The resources required for this calculation are significantly less than for a formal estimate of *e.g.*  $\chi_\nu^2$ .

A drawback of this algorithm is that it is less sensitive to non-linear ramping effects that might affect the data. Typically, these effects occur in the same population of pixels in the array, so ideally such behavior would be characterized and flagged during ground testing. The algorithm *is* sensitive to non-linear ramps to a certain extent defined by the detection threshold; the details of this sensitivity will be characterized during ground testing so it can be properly simulated in later analysis.

To detect transients, we can compute a residual function  $\Delta r_i$ :

$$\Delta r_i = (q_i - \theta_i)^2, \quad (8)$$

where  $q_i$  is defined in Equation 2 and  $\theta_i$  is a model for the expected value of the data at  $i$  based on the previous samples. To flag transients, we require  $\Delta r_i$  exceed some pre-determined threshold  $t$  times an estimate for the native variance of the time stream  $\sigma_i^2$ :

$$(q_i - \theta_i)^2 > t\sigma_i^2. \quad (9)$$

The value of  $t$  can be tuned using simulations or data (see Sec. 4.2.2). It is important that the estimate for  $\sigma_i^2$  be computed using a real-time estimate for the pixel variance, since photon noise is dominant in each integration. Since each pixel will fall on a sky position with different brightness in each integration, the photon noise will vary considerably, and a single fixed variance estimate is not appropriate.

The problem to be solved therefore reduces to developing suitable expressions for  $\theta_i$  and  $\sigma_i$ . In the absence of noise, this is trivial, with  $\theta_i = i \cdot q_{i-1}/(i-1)$  and  $\sigma_i^2 = 0$ . However, with noise in the time stream, an estimate for  $\theta_i$  based solely on  $d_{i-1}$  will be unpredictable and reduce our sensitivity to glitches. Furthermore, because the charge naturally ramps, an useful estimate for  $\sigma^2$  needs to suppress gradients in  $q(t)$ .



We can form a more reliable estimate for  $\theta_i$  by observing that it should follow an equivalent expression for Equation 2:

$$\theta_i = f \cdot i + \theta_0 \quad (10)$$

where  $\theta_0$  is some initial value of  $\theta$ . To compute this expression, we require an estimate for  $f$ , which we can write as:

$$f_i = \frac{\sum_{j=0}^i (q_j - q_0)}{\sum_{j=0}^i (j)} \quad (11)$$

If we substitute this expression straight into Equation 8, all terms will cancel. Instead, we use the sum of the  $(i - 1)$  measurements to estimate the slope, thereby reducing the error by the square root of the number of samples. That leads us to:

$$\theta_i = \left( \frac{\sum_{j=0}^{i-1} (q_j) - (i-1)q_0}{\sum_{j=0}^{i-1} (j)} \right) \cdot i + \theta_0, \quad (12)$$

and as a result:

$$\Delta r_i = (q_i - \theta_i)^2 = \left( q_i - \left\{ \left( \frac{i}{i-1} \right) \cdot \left( \sum_{j=0}^{i-1} (q_j) - (i-1)q_0 \right) + \theta_0 \right\} \right)^2. \quad (13)$$

A simplifying choice is to set  $\theta_0 = q_0$  measured for that pixel.

Computationally, this algorithm requires the storage of:

- (1)  $q_i$ , which we already have stored from the line fit;
- (2)  $i$ , which we also already have from the line fit;
- (3) the sum of the previous samples  $\sum_{j=0}^{i-1} q_j$ , which we already have from the term  $\sum q_i$  from the line fit, if we do the transient computation *before* adding  $q_i$  to  $q_{i-1}$ ; and
- (4) the initial read value  $q_0$ . This is the only new memory requirement and would have size  $4 \times 2048 \times 2048 \times 32$  bits.

In the worst case, the computation requires:

- (1) a product of two numbers  $(i - 1)$  and  $q_0$ ;
- (2) a difference between  $\sum q_{i-1}$  and the output of step 1;
- (3) a product and divide of the number computed in step 2 with  $i/(i - 1)$ ;
- (4) a sum of the output of step 3 with  $q_0$ ;
- (5) a difference between  $q_i$  and  $\theta_i$  computed in step 4;
- (6) a product of the output of step 5; and
- (7) a comparison operation between the output of the calculation and the product of a lookup value loaded in memory and  $\sigma_i^2$ .

To develop an expression for  $\sigma_i^2$ , we observe that the optimal estimate for the variance of a set of numbers  $q_i$  is given by

$$\sigma^2 = \frac{1}{n-1} \sum_{i=0}^n (q_i - \bar{q})^2 \quad (14)$$

with  $n$  as the number of samples in the set, and  $\bar{q}$  the mean of the set. In the presence of a gradient (as in Equation 2), this can be generalized to:

$$\sigma^2 = \frac{1}{n-1} \sum_{i=0}^n (q_i - (f \cdot i + q_0))^2. \quad (15)$$

The term in the parenthesis is similar to our residual estimate  $\Delta r_i$ . As a result:

$$\sigma_i^2 \approx \frac{1}{i-1} \sum_{j=0}^i \Delta r_j \quad (16)$$

We can then note that:

$$\sigma_i^2 = \frac{1}{i-1} \left( \Delta r_i + (i-2) \sum_j^{i-1} \Delta r_j \right). \quad (17)$$

This estimate requires the storage of  $4 \times 2048 \times 2048 \times 32$  bits. Since  $\Delta r_i$  is computed at each step anyway, the additional computational requirements are modest, namely:

- (1) a product of  $i-2$  and the running sum of residuals  $\sum^{i-1} \Delta r_j$ ;
- (2) a sum of  $\Delta r_i$  and the output of step 1; and
- (3) a division of the output of step 2 by  $i-1$ .

Note that, though what we term  $\sigma_i^2$  is related to the variance of the data, in fact it does not reproduce the variance calculation in an individual measurement. This is because it is formed from a running estimate of the mean, which is sensitive to deviations caused by noise.

### 3.4. *Detector Saturation*

Charge-integrating detectors have a finite well capacity, and due to mutual repulsion of electrons, also suffer from reciprocity failure at large integrated charge (*e.g.* Biesiadzinski *et al.* 2011). It is very expensive to correct this effect in real-time, since each pixel will have its own reciprocity behavior as a function of integrated charge; correction entails building a lookup table for each pixel and computing a correction factor which can be an arbitrarily complex function of  $q$ . To account for this behavior, we flag and ignore further samples for those pixels whose accumulated charge exceeds some preset threshold  $q_{\max}$ , so pixels are flagged when:

$$q_i - q_0 > q_{\max}$$

Since these quantities are stored for the photocurrent estimator, this requires no new storage requirements except for the single, global 32-bit threshold value. The value of  $q_{\max}$  can be determined pre-flight during laboratory characterization of each detector. This step does require two additional computations:

- (1) a difference of  $q_i$  and  $q_0$ ;
- (2) a comparison operation between the output of the calculation and  $q_{\max}$ .

Accurate photocurrent estimates can still be generated for these pixels, as discussed in Sec. 3.6.

### 3.5. *Early Reads*

HgCdTe arrays are known to have unpredictable behavior in the first few reads after a reset due to charge injection and other transient effects. As a result, it is desirable to include capability to ignore the first few frames in a fit (likely values run anywhere from 0 to 5). The precise number will be determined during instrument characterization; in this work, we assume a skip value of 3 frames; the results we present are not sensitive to this choice.

In addition, we have the problem that, at early frame numbers, there is not yet enough information accumulated to produce a reliable estimate for  $\sigma_i^2$ . Fortunately, if the first few reads are ignored from the fit, we can use them to generate an estimate for  $\sigma_i^2$  based on the simple difference of  $q_i$  and  $q_0$ , namely:

$$\Delta r_i = (q_i - q_0)^2. \quad (18)$$

This does not impose any additional storage or computational requirements on the algorithm.

The threshold  $t$  in Equation 9 governs the effective number of standard deviations at which a transient event is detected. In practice, we find that the algorithm is more sensitive to steps later in the time series because the variance estimate needs to be “trained” to reliably find steps. We empirically find that the training precision improves linearly with time, so we modify Equation 9 to include a weighting by the frame number as:

$$\Delta r_i = (d_i - m_i)^2 > \frac{t\sigma_i^2}{i}. \quad (19)$$

This modification effectively flattens the glitch detection efficiency. The value of  $t$  is optimized using simulations of the system (see Sec. 4.2.2).

### 3.6. Truncated Fits

For pixels suffering from cosmic ray events and saturation, it is possible to form a photocurrent estimate using the data acquired before the pixel data are flagged. In this case, we simply fit to the pre-flag data as input to the algorithm described above, using a solution to  $(A^T A)^{-1}$  appropriate for the length of data. These will be flagged as suspect in the telemetered data, and can be incorporated (or not) into later analysis as appropriate. For SPHEREx, this will allow retrieval of a photocurrent estimate for all pixels falling on bright stars with magnitudes  $J > 8$ , which occur at a rate of  $\sim 5$  per square degree in high galactic latitude fields.

## 4. Algorithm Characterization

Having developed the algorithm, we can test its performance in realistic scenarios.

### 4.1. Input Simulations

The input data simulation comprises three components. First, we simulate H2RG noise with the NGHXRG package, which simulates significant noise components including: white read noise; residual bias drifts; pink  $1/f$  noise; alternating column noise; and picture frame noise (Rauscher, 2015). In the simulation, we specify 32-output mode driven by a SIDECAR ASIC; the parameters of the simulation are specified in Table 1. Second, we simulate dark current appropriate for a typical H2RG. The current is simulated as a random draw from a Poisson distribution with mean  $i_d$ . This accurately simulates the effect of random thermal electron generation in the detectors. Finally, we simulate a flight-like photon load by generating an astrophysical image including emission from ZL, diffuse galactic light, stars, and galaxies. These components are computed in surface brightness units, and are then calibrated to photocurrent  $i_{\text{phot}}$  using Equation 1. An example input astronomical image is shown in Fig. 5. Photon noise is accounted for in the same way as for dark current, with a random draw from a Poisson distribution with mean  $i_{\text{phot}}$ . We then add cosmic rays to this simulation at a rate and with an energy spectrum determined from HST-WFC3 data as discussed in Sec. 2.1. We use statistical realizations of the measured mean cosmic ray spectrum for regular geomagnetic regions, though the algorithm performance scales to regions with increased event rates as expected.

### 4.2. Algorithm Performance

To verify the performance of the algorithm, we use the input simulated read data, propagate it through the steps described in Sec. 3, and compare the output both to the input and to the output of a standard line fitting package.

#### 4.2.1. Photocurrent Estimates

An image of both an input sky image, and the output following the on-board processing simulation is shown in Fig. 5. We find that the photocurrents are unbiased, in the sense that in the absence of instrument noise they return the input image to floating point error. Likewise, in pixels with no simulated cosmic ray

events, both our algorithm and the output of a standard fitting package<sup>8</sup> return the same values to floating point error. This satisfies requirement 1 listed in Sec. 3, since there is no discernable statistical difference between the performance of this algorithm and that of a standard line fitting algorithm under the same noise assumptions.

The assumption of constant noise required to simplify the algorithm is violated with these charge-integrating detectors since the photon noise grows in each read. However, we have tested that this algorithm still returns an unbiased estimate of the photocurrent using our simulations, and find no evidence for bias. This is due to the fact that, even though the reads toward the end of the integration are overweighted, they are not themselves biased compared to the model. If we were to use this algorithm to derive optimal fit parameter uncertainties,  $\chi^2$ , or other fit statistics sensitive to the instantaneous noise estimate we would find a significant underestimate.

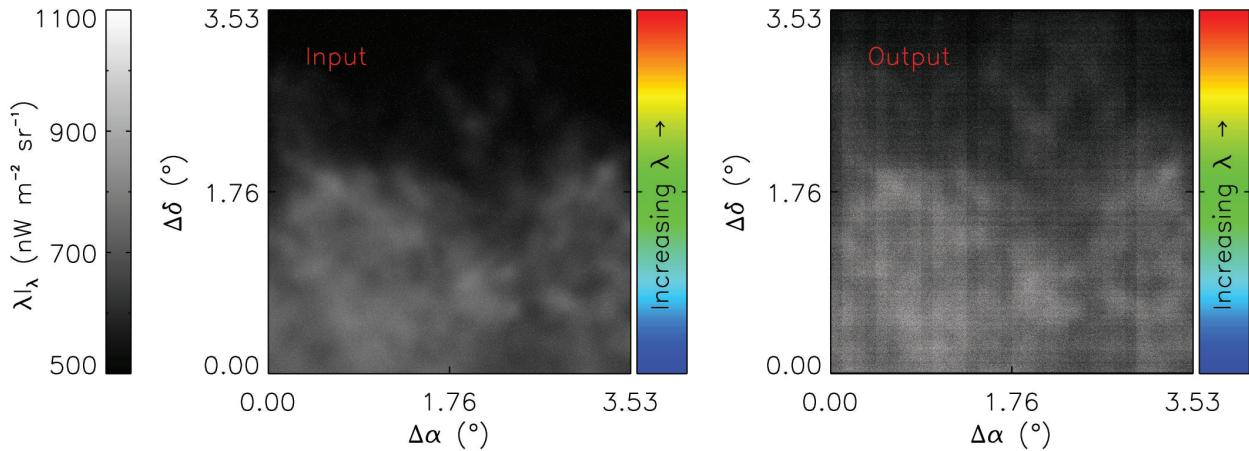


Fig. 5. Simulated SPHEREx images, both for input and after processing by the on-board photocurrent algorithm. (*LEFT*) An input sky image including emission from Zodiacal light, diffuse galactic light, stars, and galaxies for SPHEREx band 1. The image is presented as a surface brightness  $\lambda_{\lambda}$ , so that the decreasing brightness of Zodiacal light with increasing wavelength (as indicated by the bar) causes a visible gradient in the image. (*RIGHT*) Output photocurrent estimate following the addition of instrument noise, cosmic ray events, and processing by the on-board photocurrent algorithm, again expressed as  $\lambda_{\lambda}$ . The banding structure visible in the image is due to uncompensated correlated noise in the H2RG simulation. The 32 readout channels run vertically, so noise variations common to all output channels show up as horizontal stripes. We plan to compensate for these using an electronic referencing scheme similar to that presented in Moseley *et al.* (2010) in the flight system that successfully reduces the correlated noise.

#### 4.2.2. Cosmic Ray Rejection Performance

To determine the efficacy of the cosmic ray rejection algorithm, we have measured several metrics. The simplest of these is to check that images with and without cosmic ray rejection include approximately 500 fewer large-value pixels. In Fig. 6, we show the difference between a single image realization with and without cosmic ray rejection for a  $200 \times 200$  pixel sub-image. The cosmic rays are detected with high efficiency.

To maximize the performance of the algorithm, the parameter  $t$  must be optimized. We optimize against two metrics:

- *completeness*, defined as the ratio of detected events to the total number of injected cosmic rays; and
- *purity*, defined as the ratio of detected cosmic rays that were injected to all detected events.

In Fig. 7 we show the purity and completeness of the cosmic ray detection as a function of  $t$ . As expected, purity and completeness are anti-correlated. This can be understood by the fact that, as we reduce the

<sup>8</sup><http://docs.scipy.org/doc/numpy-1.10.0/reference/generated/numpy.polyfit.html>

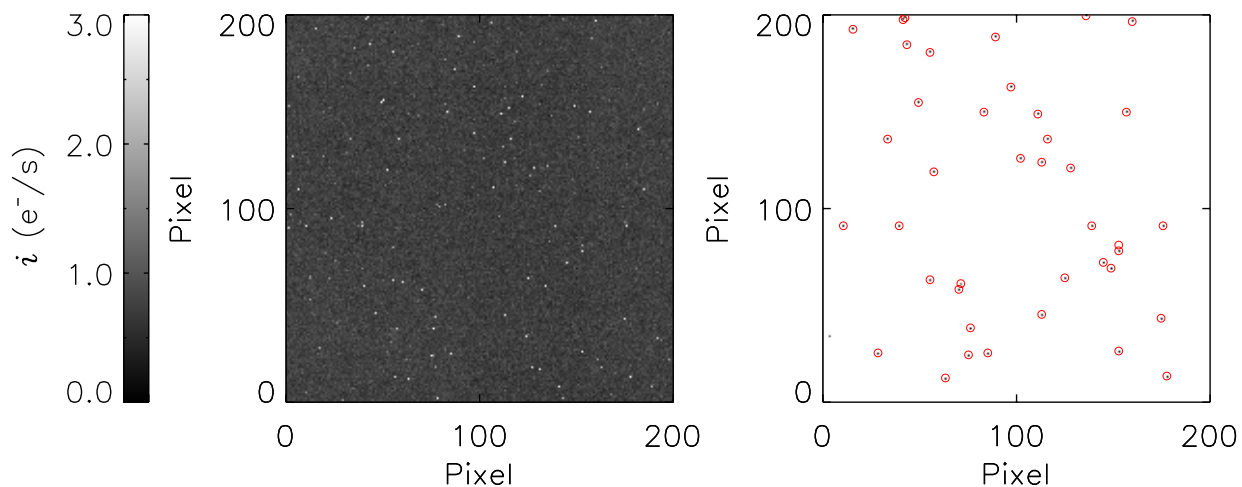


Fig. 6. Time series transient rejection visualization. (*LEFT*) A  $200 \times 200$  pixel sub-image of the simulation output (analogous to the right hand panel in Fig. 5) with no cosmic ray rejection applied. The bright pixels are due to both cosmic rays and bright stars and galaxies in the image. (*RIGHT*) The grey scale image shows the difference between photocurrent estimates with and without transient detection; cosmic rays that are found with transient detection appear as black dots. The population of input cosmic rays are also shown (red circles). Of the 40 transient events in this sub-image, 39 are found successfully, and the missed event (near  $\{5,40\}$ ) has low energy. One event is flagged with no corresponding input cosmic ray event input (near  $\{155,80\}$ ).

value of  $t$ , more candidate events will be flagged, which increases both the number of detected input events as well as the number of false detections. If we increase the value of  $t$ , the total number of detections will be reduced, which increases the number of false detections, but simultaneously missing more input cosmic rays. We find an optimum  $t_{\max} = 2500$ , where the purity is  $> 0.993$ , and the completeness is  $> 0.985$ .

The pixel loss fraction can be calculated from the purity and completeness. As shown in Fig. 8, as  $t$  is varied, the number of flagged pixels changes, with a larger loss fraction (more flagged pixels) at smaller values of  $t$ . At  $t_{\max}$ , we predict a pixel loss fraction of  $\sim 0.11\%$ , which has a negligible impact on SPHEREx science (Doré *et al.*, 2014).

Fixing to  $t = t_{\max}$ , we can investigate the performance of the cosmic ray detection algorithm versus: (i) cosmic ray energy; and (ii) time in the integration. In Fig. 9 we show a histogram of the event energies in a single simulation. Undetected cosmic ray events occur at low energies where they are more difficult to detect against the detector noise. The detection probability as a function of time is illustrated in Fig. 9. The algorithm is more likely to miss events close to the beginning of the integration because the running variance estimate has a large uncertainty during early reads (see Sec. 3.5), so cosmic ray outliers have a greater chance of passing as a normal statistical variation.

SPHEREx plans to implement both the standard 107s integration time, as well as a deeper 173s integration for use in “deep field” regions. We have simulated these longer integrations and find similar behavior to the standard length exposures. The absolute count of undetected cosmic ray events is the same, since at early reads where cosmic rays are typically missed the algorithm performance is independent of integration time. The completeness and purity of the longer integration times expressed as a fraction of total events improves since the late-time performance of the algorithm is close to ideal.

The probability of our algorithm detecting cosmic rays is largest at late times and large energies. As a result, we expect undetected cosmic rays to manifest as a slight positive-going non-Gaussianity in the flight image noise properties. Accounting for this is best handled through detailed simulation of the on-board processing using the measured flight cosmic ray rate and spectrum in the SPHEREx flight data. The resulting image simulations will need to be propagated through the full SPHEREx data reduction pipeline to build a detailed understanding of their effect on the science results (see *e.g.* Zemcov *et al.* 2014 for an example of such an analysis).

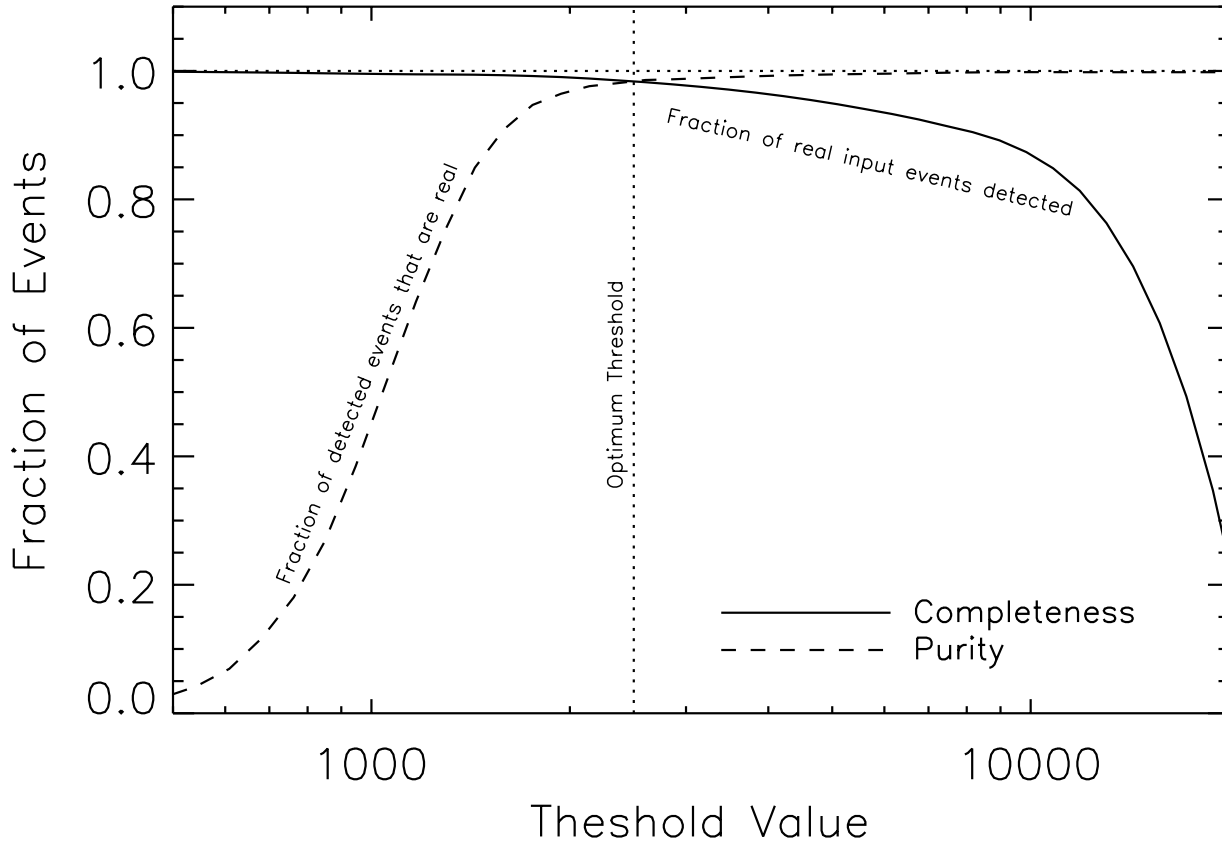


Fig. 7. The purity and completeness of the cosmic ray detection algorithm as a function of the detection threshold  $t$ , optimized at  $t_{\max} = 2500$  for a simulated  $T_{\text{int}} = 107$  s SPHEREx observation.

## 5. Hardware Implementation

The SPHEREx flight hardware provides a platform to perform on-board data analysis and reduction, as well as long-term storage prior to telemetry to the ground station.

### 5.1. Flight Processing Capabilities

The SPHEREx warm electronics uses a digital board with a Virtex 5, including 1GB SDRAM, and 128GB Flash memory for on-board data processing. The Virtex 5 performs all calculations needed for the SUR algorithm. The SDRAM provides storage of the partial sums and flag information during the exposure, and also has separate long-term storage for the final image data. Key capabilities of the Virtex 5 are 20480 Slices, 320 DSP-48s, 1.34 MB embedded RAM, and a 550MHz max clock frequency<sup>9</sup>. The warm electronics includes an additional RAD750 computer. This is used solely to compress the final images before downlink, and does not participate in the SUR calculation.

### 5.2. Implementation Tests

It is standard practice to program FPGA code and simulate its implementation in FPGA on a desktop computer. We have performed this exercise with the algorithm presented in Sec. 3 using Xilinx ISE 14.7 simulating a Virtex 5 XC5VFX130T device. The algorithm was reduced to its elementary operations and a pipeline was developed to complete the necessary calculations in hardware, as shown schematically in Fig. 10. Xilinx Coregen was used to generate p-cores that performed the arithmetic. Shift registers

<sup>9</sup>[http://www.xilinx.com/onlinestore/silicon/online\\_store\\_v5.htm](http://www.xilinx.com/onlinestore/silicon/online_store_v5.htm)

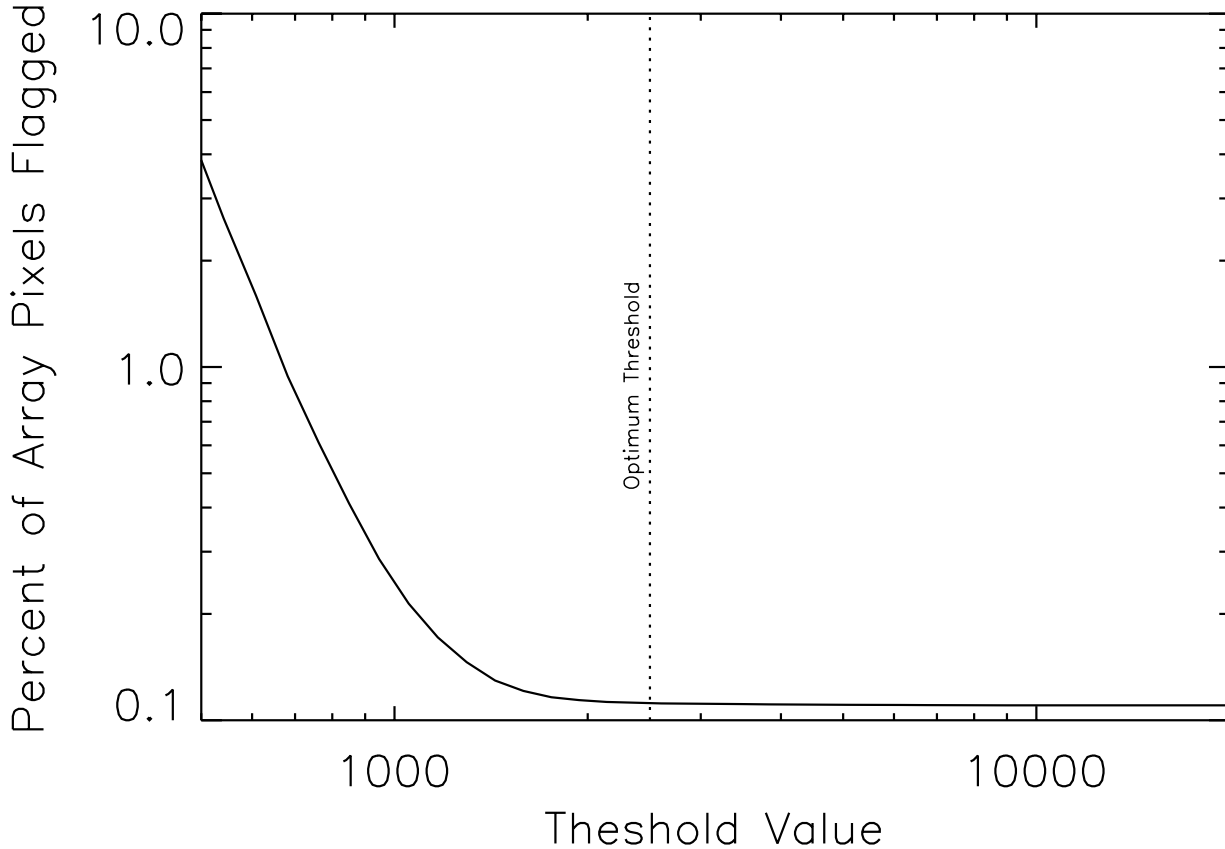


Fig. 8. Pixel flagging fraction as a function of  $t$ . At  $t_{\max}$  we predict a pixel loss fraction of  $\sim 0.11\%$  in a single integration.

and control logic were added to complete the design. Modelsim was used as the primary debugging tool throughout the development process. A sample data stream was presented to the hardware and software versions of the algorithm and both implementations returned the same slope and flag data. Because of this, we are confident that resource allocations are representative of those required in a hardware implementation of the algorithm.

### 5.2.1. FPGA Utilization

The FPGA performs calculations and operations by manipulating configurable logic blocks and utilizing on board digital signal processors (DSPs). The Virtex-5 DSP48 slices are the portions of the FPGA specifically designed for performing arithmetic. The Look-Up Table (LUT) metric represents combinational logic usage and the Flip-Flop (FF) metric represents sequential logic usage (Xilinx, 2012). The as-implemented resource utilization of the SPHEREx digital board is shown in Table 3. The FPGA utilization is at 12% or below in all respects, meaning there is ample margin, and there is room to add additional capabilities in further studies. In addition, post-synthesis analysis reported a minimum clock period of 4.390 ns. This corresponds to a maximum clock frequency of 227 MHz which easily meets the requirements of the design.

### 5.2.2. Memory Interface Utilization

Part of the main processing engine is an interface to the external memory. During the processing of the nearly 17 million pixels, each of the partial sums from Sec. 3 needs to read, manipulated, and then stored in memory every 1.5 seconds. The processing platforms must have the resources to store this data, and have bandwidth to read and write this data once every 1.5 seconds. The storage necessary to hold the partial sum, flag data, and leave space for the final image is 275 MB, and our capacity is considerably larger at

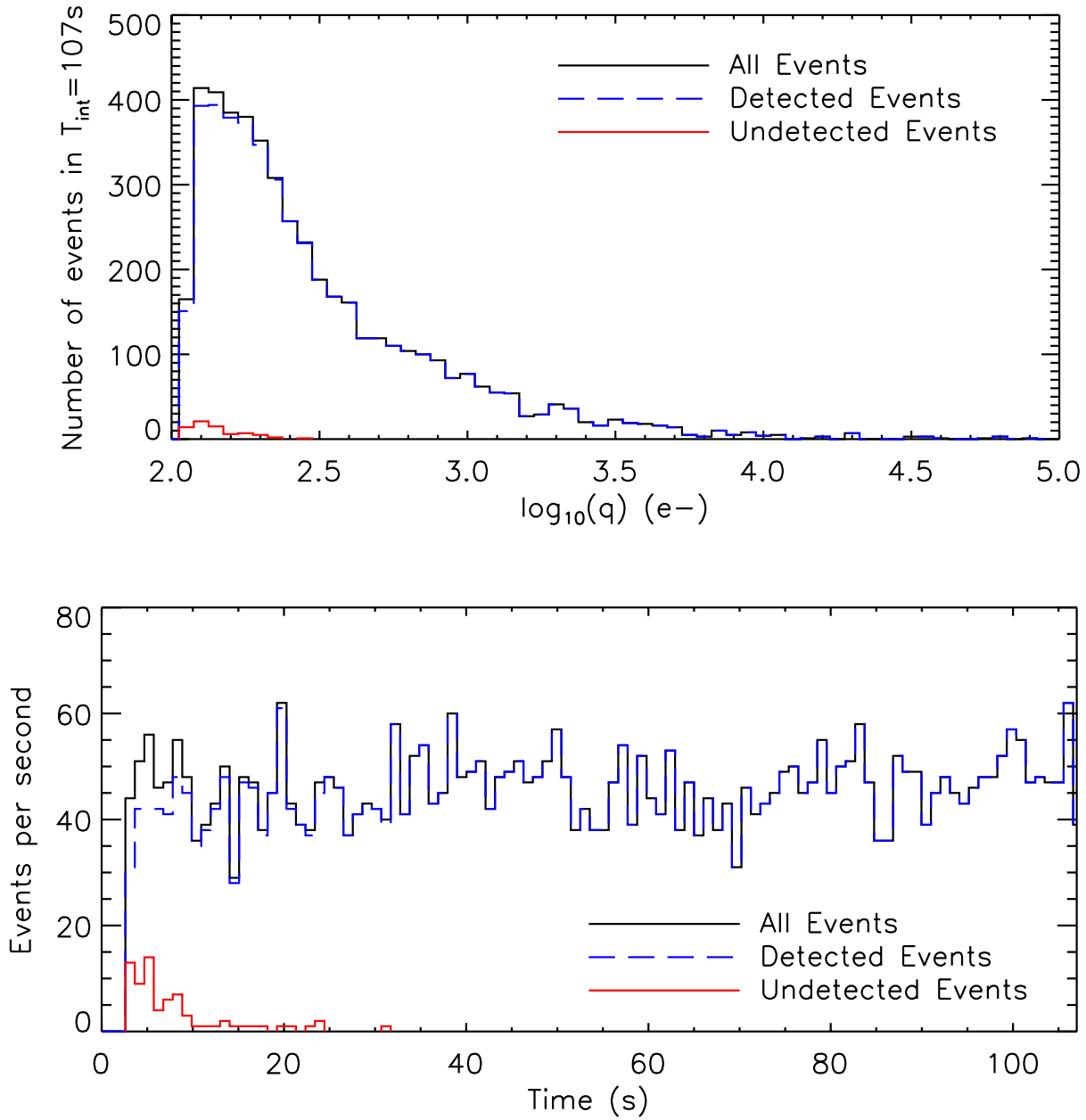


Fig. 9. Cosmic ray energy and timing diagnostics for all, detected, and undetected events. (*TOP*) Histogram of cosmic ray deposition energies in a single simulated  $T_{\text{int}} = 107\text{s}$  integration. We also indicate the population of detected events, and undetected events as indicated in the plot. In all, 98.5% of all cosmic ray events are detected. The undetected events lie at low energy where they are difficult to detect against read noise. (*BOTTOM*) Cosmic ray event times in a single simulated  $T_{\text{int}} = 107\text{s}$  integration. We indicate the population of all events, the detected events, and the undetected events as shown in the legend. Undetected events lie at early times when the error in the variance estimate used in the step detection is large. This is an unavoidable consequence of using a real-time variance estimator.





Table 3. FPGA and memory utilization by the SUR algorithm.

| Resource       | Usage | Available | Utilization [%] |
|----------------|-------|-----------|-----------------|
| DSP            | 34    | 320       | 11              |
| LUTs           | 7497  | 81920     | 9               |
| FFs            | 9746  | 81920     | 12              |
| SDRAM          | 275   | 1000      | 28              |
| Mem I/F [MB/s] | 320   | 1067      | 30              |

1 GB. The requirement on the interface is to read and write the partial sum and flag data, and yields a required rate of 320 MB per second. We compare this rate to a theoretical capacity of our SDRAM. Using 32-bit DDR SDRAM at 200 MHz with an assumed 67% bandwidth efficiency gives a capability of 1067 MB per second. This capability of 1067 MB per second is again considerably more than the required 320 MB per second.

## 6. Discussion

In this paper we provide a practical example of an on-board data processing and reduction algorithm that can fit in a resource-constrained system. Implementation of optimal photocurrent estimators are useful in similar resource-constrained systems, a salient example being CubeSats for astrophysics. Some type of on-board processing and data compression is required to fit into the limited RAM, processing capability, long-term storage, and telemetry bandwidths available in such small platforms. Our algorithm is a low-footprint, fast, hardware-demonstrated solution well suited to the needs of charge-integrating detectors, which are very common from the UV to mid-IR wavelengths. It successfully meets accuracy metrics for an optimal photocurrent estimate, and has been demonstrated in a system with flight heritage.

We have demonstrated that processing platforms with significant flight heritage are significantly underutilized by our algorithm. This provides space for other data acquisition tasks, if required, as well as showing this algorithm could fit on even more constrained platforms, if necessary. In the particular case of SPHEREx, we note there remain significant resources available to implement some form of correlated noise reduction, though part or all of the requirements for such a scheme may fall on *e.g.* the ASIC.

The algorithm discussed here has applicability beyond astrophysics, in applications as diverse as earth sensing, planetary studies, attitude control, surveillance, or any resource-constrained situation where optimal photocurrent estimates are required and time-space transients are common.

## Acknowledgments

Our sincere thanks to S. Baggett and E. Wright, who graciously sent HST-WFC3 and WISE cosmic ray data (respectively), and helped us understand how to interpret them. We would like to acknowledge the use of the NGHXRG software package written by B. Rauscher, and thank him for making such a valuable tool public.

This research was funded, in part, by the NASA Astrophysics Explorer Program. Part of this research was carried out at the Jet Propulsion Laboratory, California Institute of Technology, under a contract with the National Aeronautics and Space Administration. This publication makes use of data products from the Wide-field Infrared Survey Explorer, which is a joint project of the University of California, Los Angeles, and the Jet Propulsion Laboratory/California Institute of Technology, funded by the National Aeronautics and Space Administration, and from the NASA/ESA Hubble Space Telescope, operated by the Association of Universities for Research in Astronomy, Inc. under NASA contract NAS 5-26555.

## References

- Barker, E. A., McCullough, P. & Martel, A. R. [2010] “WFC3 IR SAA Passage Behavior,” Tech. rep., URL <http://www.stsci.edu/hst/wfc3/documents/ISRs/WFC3-2009-40.pdf>.
- Beletic, J. W., Blank, R., Gulbransen, D., Lee, D., Loose, M., Piquette, E. C., Sprafke, T., Tennant, W. E., Zandian, M. & Zino, J. [2008] “Teledyne Imaging Sensors: infrared imaging technologies for astronomy and civil space,” *High Energy, Optical, and Infrared Detectors for Astronomy III*, p. 70210H, doi:10.1117/12.790382.

- Biesiadzinski, T., Lorenzon, W., Newman, R., Schubnell, M., Tarlé, G. & Weaverdyck, C. [2011] *Publications of the Astronomical Society of the Pacific* **123**, 179, doi:10.1086/658282.
- Bock, J., Sullivan, I., Arai, T., Battle, J., Cooray, A., Hristov, V., Keating, B., Kim, M. G., Lam, A. C., Lee, D. H., Levenson, L. R., Mason, P., Matsumoto, T., Matsuura, S., Mitchell-Wynne, K., Nam, U. W., Renbarger, T., Smidt, J., Suzuki, K., Tsumura, K., Wada, T. & Zemcov, M. [2013] *The Astrophysical Journal Supplement* **207**, 32, doi:10.1088/0067-0049/207/2/32.
- Crouzet, P.-E., ter Haar, J., de Wit, F., Beaufort, T., Butler, B., Smit, H., van der Lijdt, C. & Martin, D. [2012] “Characterization of HAWAII-2RG detector and SIDECAR ASIC for the Euclid mission at ESA,” *High Energy, Optical, and Infrared Detectors for Astronomy V*, p. 84531R, doi:10.1117/12.924968.
- Doré, O., Bock, J., Ashby, M., Capak, P., Cooray, A., de Putter, R., Eifler, T., Flagey, N., Gong, Y., Habib, S., Heitmann, K., Hirata, C., Jeong, W.-S., Katti, R., Korngut, P., Krause, E., Lee, D.-H., Masters, D., Mauskopf, P., Melnick, G., Mennesson, B., Nguyen, H., Öberg, K., Pullen, A., Raccanelli, A., Smith, R., Song, Y.-S., Tolls, V., Unwin, S., Venumadhav, T., Viero, M., Werner, M. & Zemcov, M. [2014] *ArXiv e-prints 1412.4872* .
- Dressel, L. [2016] *Wide Field Camera 3 Instrument Handbook v. 8.0* (Space Telescope Science Institute).
- Fixsen, D. J., Offenber, J. D., Hanisch, R. J., Mather, J. C., Nieto-Santisteban, M. A., Sengupta, R. & Stockman, H. S. [2000] *Publications of the Astronomical Society of the Pacific* **112**, 1350, doi:10.1086/316626.
- Fowler, A. M. & Gatley, I. [1990] *The Astrophysical Journal Letters* **353**, L33, doi:10.1086/185701.
- Garnett, J. D. & Forrest, W. J. [1993] “Multiply sampled read-limited and background-limited noise performance,” *Infrared Detectors and Instrumentation*, ed. Fowler, A. M. (The SPIE), p. 395.
- Kelsall, T., Weiland, J. L., Franz, B. A., Reach, W. T., Arendt, R. G., Dwek, E., Freudenreich, H. T., Hauser, M. G., Moseley, S. H., Odegard, N. P., Silverberg, R. F. & Wright, E. L. [1998] *The Astrophysical Journal* **508**, 44, doi:10.1086/306380.
- Loose, M., Beletic, J. W., Blackwell, J., Hall, D. & Jacobsen, S. [2006] “SIDECAR ASIC - Control Electronics on a Chip,” *Astrophysics and Space Science Library*, eds. Beletic, J. E., Beletic, J. W. & Amico, P., p. 699, doi:10.1007/978-1-4020-4330-7\_85.
- Moseley, S. H., Arendt, R. G., Fixsen, D. J., Lindler, D., Loose, M. & Rauscher, B. J. [2010] “Reducing the read noise of H2RG detector arrays: eliminating correlated noise with efficient use of reference signals,” *High Energy, Optical, and Infrared Detectors for Astronomy IV*, p. 77421B, doi:10.1117/12.866773.
- Offenber, J. D., Fixsen, D. J. & Mather, J. C. [2005] *Publications of the Astronomical Society of the Pacific* **117**, 94, doi:10.1086/427566.
- Press, W. H., Teukolsky, S. A., Vetterling, W. T. & Flannery, B. P. [1992] *Numerical recipes in C. The art of scientific computing, 2nd ed.* (Cambridge University Press).
- Rauscher, B. J. [2015] *Publications of the Astronomical Society of the Pacific* **127**, 1144, doi:10.1086/684082.
- Rauscher, B. J., Alexander, D., Brambora, C. K., Derro, R., Engler, C., Fox, O., Garrison, M. B., Henegar, G., Hill, R. J., Johnson, T., Lindler, D. J., Manthripragada, S. S., Marshall, C., Mott, B., Parr, T. M., Roher, W. D., Shakoorzadeh, K. B., Smith, M., Waczynski, A., Wen, Y., Wilson, D., Xia-Serafino, W., Cabelli, C., Cheng, E., Garnett, J., Loose, M., Zandian, M., Zino, J., Ellis, T., Howe, B., Jurado, M., Lee, G., Nieznanski, J., Wallis, P., York, J., Regan, M. W., Bagnasco, G., Böker, T., De Marchi, G., Ferruit, P., Jakobsen, P. & Strada, P. [2007] “Detector arrays for the James Webb Space Telescope near-infrared spectrograph,” *Focal Plane Arrays for Space Telescopes III*, p. 66900M, doi:10.1117/12.731759.
- Robberto, M. [2007] “Analysis of the sampling schemes for WFC3-IR,” Tech. rep.
- Smith, R. M. & Hale, D. [2012] “Read noise for a 2.5 $\mu$ m cutoff Teledyne H2RG at 1-1000Hz frame rates,” *High Energy, Optical, and Infrared Detectors for Astronomy V*, p. 84530Y, doi:10.1117/12.927148.
- Spangelo, S. C., Katti, R. M., Unwin, S. C. & Bock, J. J. [2015] *Journal of Astronomical Telescopes, Instruments, and Systems* **1**, 037001, doi:10.1117/1.JATIS.1.3.037001.
- Wright, E. L., Eisenhardt, P. R. M., Mainzer, A. K., Ressler, M. E., Cutri, R. M., Jarrett, T., Kirkpatrick, J. D., Padgett, D., McMillan, R. S., Skrutskie, M., Stanford, S. A., Cohen, M., Walker, R. G., Mather, J. C., Leisawitz, D., Gautier, T. N., III, McLean, I., Benford, D., Lonsdale, C. J., Blain, A., Mendez, B., Irace, W. R., Duval, V., Liu, F., Royer, D., Heinrichsen, I., Howard, J., Shannon, M., Kendall, M., Walsh, A. L., Larsen, M., Cardon, J. G., Schick, S., Schwalm, M., Abid, M., Fabinsky, B., Naes, L. & Tsai, C.-W. [2010] *Astronomical Journal* **140**, 1868-1881, doi:10.1088/0004-6256/140/6/1868.
- Xilinx [2012] *Virtex-5 FPGA User Guide* (Xilinx, Inc.).
- Zemcov, M., Smidt, J., Arai, T., Bock, J., Cooray, A., Gong, Y., Kim, M. G., Korngut, K., Lam, A., Lee, D. H., Matsumoto, T., Matsuura, S., Nam, U. W., Roudier, G., Tsumura, K. & Wada, T. [2014] *Science* **346**, 6210.